

## The topographic effect of ground motion based on Spectral Element Method

Xinrong Liu<sup>1,2a</sup>, Meihai Jin<sup>1,2b</sup>, Dongliang Li<sup>\*1,2</sup>,  
Yuanxin Hu<sup>1,2b</sup> and Jianxue Song<sup>1,2c</sup>

<sup>1</sup> School of Civil Engineering, Chongqing University, Chongqing 400045, China

<sup>2</sup> Key Laboratory of New Technology for Construction of Cities in Mountain Area (Chongqing University),  
Ministry of Education, Chongqing

(Received May 20, 2016, Revised February 18, 2017, Accepted March 23, 2017)

**Abstract.** A Spectral Element Method for 3D seismic wave propagation simulation is derived based on the three-dimensional fluctuating elastic dynamic equation. Considering the 3D real terrain and the attenuation characteristics of the medium, the topographic effect of Wenchuan earthquake is simulated by using the Spectral Element Method (SEM) algorithm and the ASTER DEM model. Results show that the high PGA (peak ground acceleration) region was distributed along the peak and the slope side away from the epicenter in the epicenter area. The overall distribution direction of high PGA and high PGV (peak ground velocity) region is parallel to the direction of the seismogenic fault. In the epicenter of the earthquake, the ground motion is to some extent amplified under the influence of the terrain. The amplification effect of the terrain on PGA is complicated. It does not exactly lead to amplification of PGA at the ridge and the summit or attenuation of PGA in the valley.

**Keywords:** topographic effect; Spectral Element Method; seismogenic; peak ground acceleration; peak ground velocity; peak ground displacement

---

### 1. Introduction

The distribution patterns of ground motion can provide important information for the study of earthquake-induced secondary geological disasters. A lot of researches have been done on the topographic effect of ground motion. Todorovska *et al.* (2015) studied the effects of the site conditions using synthetic earthquake ground motion at the ground surface, generated by the SYNACC method. Rizzitano *et al.* (2014) confirmed that a complex interaction existed between stratigraphic and topographic effects on the amplification of the ground motion and that the two effects cannot be evaluated independently and easily uncoupled. Barani *et al.* (2014) examined the role of topographic effects on the prediction of earthquake ground motion. Using landslide maps from the epicentral area of earthquakes near Northridge, California, Chi-Chi, Taiwan, and the Finisterre Mountains of Papua New Guinea, Meunier *et al.* (2008) investigated the control of these

---

\*Corresponding author, Ph.D., E-mail: [myheartwillgoon17@126.com](mailto:myheartwillgoon17@126.com)

<sup>a</sup> Ph.D., Professor

<sup>b</sup> Ph.D.

<sup>c</sup> M.S.

site effects over the location of earthquake-induced slope failure. In these examples, earthquake-triggered landslides clustered near ridge crests, where the susceptibility to landsliding was greatest. Topographic effect and other aspects of ground motion were also analyzed and interpreted in these studies. However, the calculations were based on two-dimensional equivalent model of terrain, and the real three-dimensional topographic effect of ground motion was rarely involved.

The calculation of topographic effect should be started by solving the seismic wave field. Because of the computational complexity of the seismic wave field, only a small number of analytic solutions of the regular terrain can be obtained (Zhang *et al.* 2015, Gao and Zhang 2013). Therefore, numerical methods are adopted in the computation of seismic wave field, such as Finite Difference Method (FDM) (Shao and Ma 2016), Finite Element Method (FEM) (Gao and Zhao 2016), Boundary Element method (BEM) (Gao *et al.* 2016, Zhao *et al.* 2015, Liu *et al.* 2016), Pseudo-Spectral Method (PSM) (Chaljub *et al.* 2015, Sukan and Vuan 2014) and Spectral Element Method (SEM) (Liu *et al.* 2015), etc. Among these methods, SEM belongs to the generalized finite element method and was first used in fluid dynamics calculations. Based on the integration of PSM with FEM, it takes full advantage of the high precision and rapid convergence speed of the former, and the geometric flexibility of the latter, reducing the computation load and data storage demands (Tarinejad and Pirboudaghi 2015), and making high-efficiency parallel computing possible (Galvez *et al.* 2014). SEM not only can be used to calculate 2D and 3D seismic wave field in inhomogeneous media and complex geological body, also can be used to simulate the propagation of seismic waves in the world.

Due to the above advantages of SEM in seismic wave field simulation, the Spectral Element Method algorithm is derived in this paper on the basis of three-dimensional fluctuating elastic dynamic equation. By combining this method with the ASTER DEM model, the real 3D topographic effect of ground motion in Longmen Mountain area caused by the Wenchuan earthquake is simulated, and the distribution of high PGA region and high PGV region is studied.

## 2. 3-D seismic wave propagation modeling based on SEM

The fundamental purpose of establishing the propagation model of seismic wave is to solve the equations of motion in a continuous medium characterized by displacement (velocity and acceleration). In general expression of the elastic theory, displacement of an element within the medium is connected with stress and external force acting on the element. Thus, the three-dimensional fluctuating elastic dynamic equation of an element is (Udías 2008, Yan *et al.* 2009)

$$\rho(\mathbf{x}) \cdot \frac{\partial^2}{\partial t^2} \mathbf{u}(\mathbf{x}, t) - \nabla \cdot \boldsymbol{\sigma}(\mathbf{x}, t) = \mathbf{f}(\mathbf{x}, t) \quad (1)$$

Where  $\rho(\mathbf{x})$  is the mass,  $\mathbf{u}(\mathbf{x}, t)$  is the displacement field,  $\boldsymbol{\sigma}(\mathbf{x}, t)$  is the stress field,  $\nabla$  is  $\partial/\partial \mathbf{x}$  and  $\mathbf{f}(\mathbf{x}, t)$  represents seismic source. The formula is expressed as a component of  $\mathbf{u}$ , that is

$$\rho \frac{\partial^2 u_i}{\partial t^2} - \frac{\partial \sigma_{ij}}{\partial x_j} = f_i (\forall i = 1, 2, 3) \quad (2)$$

Or  $\rho \ddot{u}_i - \sigma_{ij,j} = f_i (\forall i = 1, 2, 3)$ , where  $\sigma_{ij,j}$  is the derivative of  $\sigma_{ij}$  in the direction of  $j$ , and  $\sigma_{ij}$  is obtained according to the Hooke's law

$$\sigma_{ij} = c_{ijkl} \epsilon_{kl} = c_{ijkl} u_{k,l} \tag{3}$$

Based on the above three formulas, the basic algorithm of SEM can be derived.

### 2.1 The weak form of three-dimensional fluctuating elastic dynamic equation

Fig. 1 is the schematic diagram of SEM calculation model. In the figure,  $\Omega$  represents the model domain,  $\partial\Omega$  represents the free boundary surface,  $\Gamma$  represents the absorbing boundary surface, and  $\hat{n}$  is the normal vector of each boundary. The seismic trigger source  $\mathbf{x}_s$  can be located anywhere within  $\Omega$  (Komatitsch and Tromp 1999). By multiplying both ends of Eq. (1) by the test vector  $\mathbf{w}(\mathbf{x})$  and integration in the whole model domain, the following is obtained:

$$\int_{\Omega} \mathbf{w} \rho \ddot{\mathbf{u}} d\mathbf{x} - \int_{\Omega} \mathbf{w} \nabla \cdot \boldsymbol{\sigma} d\mathbf{x} = \int_{\Omega} \mathbf{w} \mathbf{f} d\mathbf{x} \tag{4}$$

The second item on the left side of Eq. (4) is integrated in the model domain and the model boundary

$$\int_{\Omega} \mathbf{w} \rho \ddot{\mathbf{u}} d\mathbf{x} - \int_{\Gamma} \mathbf{w} \nabla \cdot \boldsymbol{\sigma} d\mathbf{x} + \int_{\Omega} \nabla \mathbf{w} \boldsymbol{\sigma} d\mathbf{x} = \int_{\Omega} \mathbf{w} \mathbf{f} d\mathbf{x} \tag{5}$$

$\sigma_{\partial\Omega}$  on the free boundary  $\partial\Omega$  is 0; and  $\sigma_G$  on the absorbing boundary  $\Gamma$  can be expressed as

$$\boldsymbol{\sigma}_G = \rho \mathbf{v} \hat{\mathbf{n}} \tag{6}$$

Where  $\mathbf{v}$  is velocity. Then Eq. (5) becomes

$$\int_{\Omega} \mathbf{w} \rho \ddot{\mathbf{u}} d\mathbf{x} - \int_{\Gamma} \mathbf{w} \nabla \rho \mathbf{v} \hat{\mathbf{n}} d\mathbf{x} + \int_{\Omega} \nabla \mathbf{w} \boldsymbol{\sigma} d\mathbf{x} = \int_{\Omega} \mathbf{w} \mathbf{f} d\mathbf{x} \tag{7}$$

This formula is the weak form of the integral form of Eq. (1), and the right side of it represents the seismic source.

Eq. (7) is suitable for any test vector  $\mathbf{w}(\mathbf{x})$ , and it meets the natural boundary condition. Therefore, it is relatively easy to process the free surface boundary. However, the selection of test vector should be made wherever possible so that the theoretical analysis and numerical calculation are easier. Compared with the surface wave simulation results based on strong form, Eq. (7) is

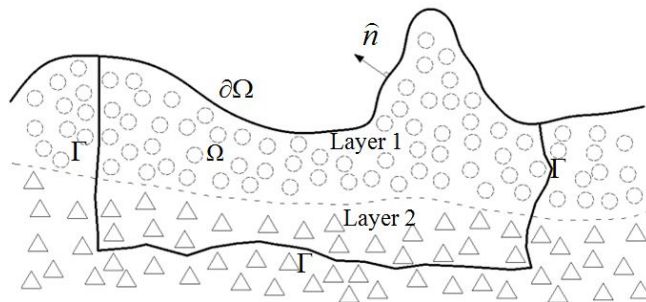
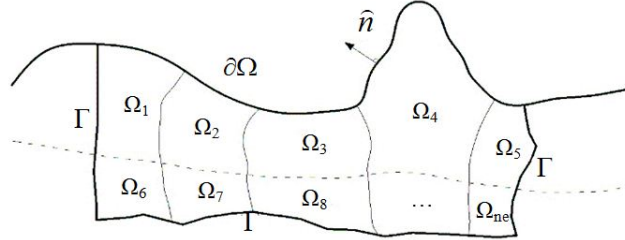


Fig. 1 Schematic diagram of SEM calculation model

Fig. 2 Sub-domains  $\Omega_e$  in the model domain  $\Omega$ 

more accurate (Yoshimatsu and Abe 2006).

## 2.2 Domain discretion and mapping functions

Combined with various types of geological interface in the model domain  $\Omega$  (Komatitsch and Tromp 2002),  $\Omega$  is divided into  $n_e$  sub-domains (Fig. 2), and  $\Omega = \bigcup_e^{n_e} \Omega_e$ . If the sub-domains are 2D, they are discretized into quadrilateral elements; if 3D, they are discretized into hexahedral elements.

Based on Fig. 2, the weak form of the integral form of the motion equations for each sub-domain can be expressed as follows

$$\int_{\Omega^e} \mathbf{w} \rho \ddot{\mathbf{u}} d\mathbf{x} - \int_{\Gamma} \mathbf{w} \nabla \rho \mathbf{v} \mathbf{u} d\mathbf{x} + \int_{\Omega^e} \nabla \mathbf{w} \boldsymbol{\sigma} d\mathbf{x} = \int_{\Omega^e} \mathbf{w} \mathbf{f} d\mathbf{x} \quad e = 1, 2, \dots, n_e \quad (8)$$

Each unit sub-domain  $\Omega_e$  is mapped to the three-dimensional local coordinate system  $\Lambda_3 = \Lambda = \Lambda \otimes \Lambda \otimes \Lambda$ , where  $\otimes$  is tensor product and  $\Lambda \in [-1, 1]$ . Then the mapping function  $F_e: \Lambda \rightarrow \Omega_e$  is defined by the following formula

$$\begin{cases} F_e(\xi) = \mathbf{x}_e(\xi) = \sum_{a=1}^{n_a} N_a(\xi) \mathbf{x}_a^e \\ \mathbf{x}_e(\xi, \eta, \zeta) = \sum_{a=1}^{n_a} N_a(\xi, \eta, \zeta) \mathbf{x}_a^e \end{cases} \quad (9)$$

Where  $\mathbf{x}_a^e$  is the  $n_a$ th control point of  $e$ th element. According to the order  $N$  of Lagrange polynomial, the 3D element may contain eight control points ( $N = 1$ ) or 27 control points ( $N = 2$ ), as shown in Fig. 3. The control points of each hexahedral surface center and hexahedral center are often ignored in actual calculation, so there are a total of 20 control points (the filled circles in Fig. 3(b)).

For a hexahedral element,  $\hat{\mathbf{n}}$  of each face exists. According to Eq. (9), Jacobi matrix  $\mathbf{J}^e$  of the element is a  $3 \times 3$  matrix, and can be obtained by taking the derivative of Eq. (9)

$$\mathbf{J}^e = dF_e(\xi)/d\xi = d\mathbf{x}^e(\xi)/d\xi = \sum_{a=1}^{n_a} \frac{dN_a(\xi)}{d\xi} \mathbf{x}_a^e \quad (10)$$

The whole matrix form of Eq. (10) is



Fig. 3 Control points on the surface of hexahedral elements

$$\mathbf{J}^e = \begin{pmatrix} \frac{\partial_x(\xi)}{\partial\xi} & \frac{\partial_x(\xi)}{\partial\eta} & \frac{\partial_x(\xi)}{\partial\zeta} \\ \frac{\partial_y(\xi)}{\partial\xi} & \frac{\partial_y(\xi)}{\partial\eta} & \frac{\partial_y(\xi)}{\partial\zeta} \\ \frac{\partial_z(\xi)}{\partial\xi} & \frac{\partial_z(\xi)}{\partial\eta} & \frac{\partial_z(\xi)}{\partial\zeta} \end{pmatrix} \quad (11)$$

Let  $\mathfrak{J}^e = \det \mathbf{J}^e$ , and

$$\mathfrak{J}^e = \frac{\partial(x, y, z)}{\partial(\xi, \eta, \zeta)} = \begin{vmatrix} \frac{\partial_x(\xi)}{\partial\xi} & \frac{\partial_x(\xi)}{\partial\eta} & \frac{\partial_x(\xi)}{\partial\zeta} \\ \frac{\partial_y(\xi)}{\partial\xi} & \frac{\partial_y(\xi)}{\partial\eta} & \frac{\partial_y(\xi)}{\partial\zeta} \\ \frac{\partial_z(\xi)}{\partial\xi} & \frac{\partial_z(\xi)}{\partial\eta} & \frac{\partial_z(\xi)}{\partial\zeta} \end{vmatrix} \quad (12)$$

Eq. (12) describes the volume change in the element when a hexahedral element in the global coordinate is mapped to the local coordinate, that is

$$dxdydz = \mathfrak{J}^e d\xi d\eta d\zeta \quad (13)$$

### 2.3 Interpolation function of element

Lagrange interpolation of three-dimensional element is carried out independently along each coordinate direction. It can be expressed in the form of tensor product

$$L_{ijk}^N = \ell_i^N \otimes \ell_j^N \otimes \ell_k^N \quad (14)$$

Where  $N$  is the order of the Lagrange polynomial, and 1 is Lagrange operator. In order to meet the accuracy requirement of SEM, High-end ( $4 \leq N \leq 8$ ) Lagrange polynomial is used to interpolate (Komatitsch and Tromp 1999).

For a scalar function  $g$ , its 3D interpolation is

$$g(\xi) \approx \sum_{i,j,k=0}^N g(\xi_i, \eta_j, \zeta_k) L_{ijk}^N(\xi) \quad (15)$$

By substituting Eq. (14) into Eq. (15), the following is obtained

$$\begin{aligned} g(\xi) &\approx \sum_{i,j,k=0}^N g(\xi_i, \eta_j, \zeta_k) l_i(\xi) \otimes l_j(\eta) \otimes l_k(\zeta) \\ &= \sum_{i,j,k=0}^N g(\xi_i, \eta_j, \zeta_k) l_i(\xi) l_j(\eta) l_k(\zeta) \\ &= \sum_{i,j,k=0}^N g_{ijk} l_i(\xi) l_j(\eta) l_k(\zeta) \end{aligned} \quad (16)$$

According to the nature of the Lagrange polynomial

$$l_i(\xi_j) = \delta_{ij} \quad (17)$$

Therefore

$$L_{ijk}^N(\xi_l, \eta_m, \zeta_n) = \delta_{il} \delta_{jm} \delta_{kn} \quad (18)$$

For a vector with three components, its interpolation is

$$\begin{aligned} \mathbf{u}^e(\xi) &\approx \sum_{i=1}^3 \hat{\xi}_l \sum_{i,j,k=0}^N \mathbf{u}^e(\xi_i, \eta_j, \zeta_k) l_i(\xi) l_j(\eta) l_k(\zeta) \\ &= \sum_{i=1}^3 \hat{\xi}_l \sum_{i,j,k=0}^N \mathbf{u}_{ijk}^e l_i(\xi) l_j(\eta) l_k(\zeta) \end{aligned} \quad (19)$$

According to Eqs. (17)-(18), the value of Lagrange polynomial at the control point  $\xi_{ijk} = (\xi_i, \eta_j, \zeta_k)$  is 1. Therefore, after the interpolation, Eq. (19) is true for control point  $\xi_{ijk}$ . The partial derivative of Eq. (19) is

$$\left. \begin{aligned} \frac{\partial \mathbf{u}^e(\xi)}{\partial \xi} &= \partial_{\xi} \mathbf{u}^e(\xi, \eta, \zeta) \\ &\approx \sum_{i,j,k=0}^N \mathbf{u}_{ijk}^e l'_i(\xi) l_j(\eta) l_k(\zeta) \\ \frac{\partial \mathbf{u}^e(\xi)}{\partial \eta} &= \partial_{\eta} \mathbf{u}^e(\xi, \eta, \zeta) \\ &\approx \sum_{i,j,k=0}^N \mathbf{u}_{ijk}^e l_i(\xi) l'_j(\eta) l_k(\zeta) \\ \frac{\partial \mathbf{u}^e(\xi)}{\partial \zeta} &= \partial_{\zeta} \mathbf{u}^e(\xi, \eta, \zeta) \\ &\approx \sum_{i,j,k=0}^N \mathbf{u}_{ijk}^e l_i(\xi) l_j(\eta) l'_k(\zeta) \end{aligned} \right\} \quad (20)$$

Gradient of the scalar function  $g$  in the global coordinate system  $\mathbf{x}$  can be determined by the following formula

$$\begin{aligned} \nabla_{\mathbf{x}} g(\mathbf{x}(\xi)) &\approx \sum_{l=1}^3 \hat{\mathbf{x}}_l \partial_l g(\mathbf{x}(\xi, \eta, \zeta)) \\ &= \sum_{l=1}^3 \hat{\mathbf{x}}_l \sum_{i,j,k=0}^N g_{ijk} \begin{bmatrix} \ell'_i(\xi) \ell_j(\eta) \ell_k(\zeta) \partial_l \xi \\ + \ell_l(\xi) \ell'_j(\eta) \ell_k(\zeta) \partial_l \eta \\ + \ell_l(\xi) \ell_j(\eta) \ell'_k(\zeta) \partial_l \zeta \end{bmatrix} \end{aligned} \quad (21)$$

With the inverse matrix  $\partial_l \xi = \partial \xi / \partial x_l$  of Jacobi matrix, when calculating any GLL (Gauss Lobatto Legendr) point  $\mathbf{x}(\xi_\alpha, \eta_\beta, \zeta_\gamma)$ , Eq. (21) can be simplified to

$$\begin{aligned} \nabla_{\mathbf{x}} g(\mathbf{x}(\xi_\alpha, \eta_\beta, \zeta_\gamma)) &\approx \sum_{l=1}^3 \hat{\mathbf{x}}_l \begin{bmatrix} \sum_{i=0}^N g_{i\beta\gamma} \ell'_i(\xi_\alpha) \partial_l \xi(\xi_\alpha, \eta_\beta, \zeta_\gamma) \\ + \sum_{j=0}^N g_{\alpha j \gamma} \ell'_j(\eta_\beta) \eta(\xi_\alpha, \eta_\beta, \zeta_\gamma) \\ + \sum_{k=0}^N g_{\alpha\beta k} \ell'_k(\zeta_\gamma) \zeta(\xi_\alpha, \eta_\beta, \zeta_\gamma) \end{bmatrix} \end{aligned} \quad (22)$$

It should be noted that Eq. (22) is true only when  $\mathfrak{J}^e \neq 0$  (i.e.,  $\mathbf{J}^e$  is a nonsingular matrix). Eq. (22) also shows that in the inverse mapping from the local coordinates to global coordinates, 9 components of  $\mathbf{J}^e$  should be calculated, which are  $\partial \xi_i / \partial x_j$  ( $i, j = 1, 2, 3$ ), where  $\xi_1 = \xi$ ,  $\xi_2 = \eta$  and  $\xi_3 = \zeta$ .

#### 2.4 Element mass matrix and force calculation

In order to obtain the diagonalizable mass matrix of element, the GLL integration is needed. The integration rule is as follows

$$\begin{aligned} \int_{\Lambda} g(\xi) d\xi &= \int_{-1}^1 \int_{-1}^1 \int_{-1}^1 g(\xi, \eta, \zeta) d\xi d\eta d\zeta \\ &\approx \sum_{i,j,k=0}^N \omega_i \omega_j \omega_k g(\xi_i, \eta_j, \zeta_k) \\ &= \sum_{i,j,k=0}^N \omega_i \omega_j \omega_k g_{ijk} \end{aligned} \quad (23)$$

Where  $\omega_i$  is the weight of GLL integration;  $g(\xi)$  is an arbitrary function defined in  $\Lambda \in [-1, 1]$ ,  $g_{ijk}$  is the abbreviation of  $g(\xi_i, \eta_j, \zeta_k)$  and  $J_{ijk}^e$  is the abbreviation of  $J^e(\xi, \eta, \zeta)$ . GLL integration is accurate for polynomials with an order not more than  $2N-1$ . For a homogeneous element without deformation, GLL integration also involves the product of two  $N$  order polynomials, one derived

from the interpolation of displacement, and the other derived from the test function or vectors. Therefore, integral of 2N-order polynomial has certain errors, especially for the solving of the inhomogeneous medium and deformation elements. However, such errors can be ignored in the SEM in order to obtain the element's mass matrix with a diagonal structure (Komatitsch and Tromp 1999).

The inner product of test vector  $\mathbf{w}$  and displacement field  $\mathbf{u}$  is

$$\mathbf{w} \cdot \mathbf{u} = \sum_{i,j=1}^3 w_i u_j \hat{\mathbf{x}}_i \cdot \hat{\mathbf{x}}_j = \sum_{i,j=1}^3 w_i u_j \delta_{ij} = \sum_{i=1}^3 w_i u_i \quad (24)$$

So the test function can be set to  $w = (\delta_{1i}, \delta_{2i}, \delta_{3i})$  for each displacement component  $u_i$ , and each displacement component can be calculated separately. Similarly, the inner product of the other two vectors of Eq. (8) can be treated in the same way. Thus, integration of the first item on the left side of Eq. (8) is

$$\begin{aligned} & \int_{\Omega^e} \rho(\mathbf{x}) \mathbf{w}(\mathbf{x}) \ddot{\mathbf{u}}(\mathbf{x}) d\mathbf{x} \\ &= \int_{\Lambda} \rho(\xi) \mathbf{w}(\xi) \ddot{\mathbf{u}}(\xi) d\xi \\ &\approx \sum_{r,s,t=0}^N \left\{ \rho_{rst} \omega_r \omega_s \omega_t \left[ \sum_{i,j,k=0}^N w_{ijk} \ell_i(\xi_r) \ell_j(\eta_s) \ell_k(\zeta_t) \right] \right. \\ &\quad \left. \cdot \left[ \sum_{l,m,n=0}^N \ddot{u}_{lmn} \ell_l(\xi_r) \ell_m(\eta_s) \ell_n(\zeta_t) \right] \mathfrak{T}_{rst} \right\} \end{aligned} \quad (25)$$

During the derivation of Eq. (25), the coordinate mapping and interpolation of Jacobi matrix, and GLL integration are used. In order to simplify the calculation formula, Terms similar to  $u(\xi_i, \eta_m, \zeta_n)$  are represented by  $u_{lmn}$  and  $\omega_r \omega_s \omega_t$  in Eq. (25) is abbreviated to  $\omega_{rst}$ . Because the test function is an arbitrary function, let  $w_{ijk} = 1$ , and the above formula can be further simplified as

$$\begin{aligned} & \sum_{r,s,t=0}^N \left\{ \rho_{rst} \omega_r \omega_s \omega_t \left[ \sum_{i,j,k=0}^N v_{ijk} \ell_i(\xi_r) \ell_j(\eta_s) \ell_k(\zeta_t) \right] \right. \\ & \quad \left. \cdot \left[ \sum_{l,m,n=0}^N \ddot{u}_{lmn} \ell_l(\xi_r) \ell_m(\eta_s) \ell_n(\zeta_t) \right] \mathfrak{T}_{rst} \right\} \\ &= \sum_{l,m,n=0}^N \left\{ \ddot{u}_{lmn} \left[ \sum_{i,j,k=0}^N \sum_{r,s,t=0}^N \rho_{rst} \omega_{rst} \mathfrak{T}_{rst} \delta_{ir} \delta_{js} \delta_{kt} \delta_{lr} \delta_{ms} \delta_{nt} \right] \right\} \\ &= \sum_{l,m,n=0}^N \ddot{u}_{lmn} \sum_{i,j,k=0}^N \rho_{ijk} \omega_{ijk} \mathfrak{T}_{ijk} \delta_{li} \delta_{mj} \delta_{nk} \\ &= \sum_{l,m,n=0}^N \ddot{u}_{lmn} \sum_{i,j,k=0}^N \rho_{ijk} \omega_{ijk} \mathfrak{T}_{ijk} \delta_{(lmn)(ijk)} \end{aligned} \quad (26)$$

$$= \sum_{\alpha=1}^{(N+1)^3} \ddot{u}_{\alpha} \sum_{\beta=1}^{(N+1)^3} \rho_{\beta} \omega_{\beta} \mathfrak{S}_{\beta} \delta_{\alpha\beta} = \ddot{u}_{\alpha} M_{\alpha\beta}^e \quad (26)$$

Where  $\alpha = lmn, \beta = ijk, \beta = 1, \dots, (N + 1)^3, \alpha$  and  $\delta_{(lmn)(ijk)} = \delta_{li} \delta_{mj} \delta_{nk}$ .

In this equation,  $M_{\alpha\beta}^e$  is the mass matrix of an element, which can be expressed as the product of the mass  $\rho$  of the point  $(\zeta_i, \eta_j, \zeta_k)$ , Jacobi determinant and weight of GLL integration.

$$M_{\alpha\beta}^e = \rho_{\beta} \omega_{\beta} \mathfrak{S}_{\beta} \delta_{\alpha\beta} = \rho_{ijk} \omega_{ijk} \mathfrak{S}_{ijk} \quad (\forall i, j, k = 0, \dots, N) \quad (27)$$

According to Eq. (26), the relationship between  $\alpha, \beta$  and  $ijk$  can be expressed as

$$\alpha(\beta) = \sum_{i,j,k=0}^N (i+1) \cdot (j+1) \cdot (k+1) \quad (28)$$

The element stiffness matrix  $K^e$  can be obtained by the integral of the third item on the left side of Eq. (8), the derivation of which is similar to that of Eqs. (25)-(26) and (28).

### 2.5 Node force of element

To calculate the node force of an element, nine elements of the strain tensor of the given point  $\xi_{\alpha\beta\gamma} = (\xi_{\alpha}, \xi_{\beta}, \xi_{\gamma})$  should be determined. According to the displacement gradient  $\nabla \mathbf{u}$

$$\begin{aligned} \partial_i u_{(j)}(\mathbf{x}(\xi_{\alpha\beta\gamma})) &\approx \left[ \sum_{l=0}^N u_{(j)l\beta\gamma} \ell'_l(\xi_{\alpha}) \right] \partial_i \xi(\xi_{\alpha}, \eta_{\beta}, \zeta_{\gamma}) \\ &+ \left[ \sum_{m=0}^N u_{(j)\alpha m\gamma} \ell'_m(\eta_{\beta}) \right] \partial_i \eta(\xi_{\alpha}, \eta_{\beta}, \zeta_{\gamma}) + \left[ \sum_{n=0}^N u_{(j)\alpha\beta n} \ell'_n(\zeta_{\gamma}) \right] \partial_i \zeta(\xi_{\alpha}, \eta_{\beta}, \zeta_{\gamma}) \end{aligned} \quad (29)$$

Where  $u_{(j)\alpha\beta\gamma}$  is the  $j$ th element of the displacement vector of  $\xi_{\alpha\beta\gamma} = (\xi_{\alpha}, \xi_{\beta}, \xi_{\gamma})$ . According to Eq. (3), the stress tensor at this point is

$$\boldsymbol{\sigma}(\mathbf{x}(\xi_{\alpha\beta\gamma})) = \mathbf{c}(\mathbf{x}(\xi_{\alpha\beta\gamma})) \otimes \nabla \mathbf{u}(\mathbf{x}(\xi_{\alpha\beta\gamma})) \quad (30)$$

$\nabla \mathbf{w} \cdot \boldsymbol{\sigma}$  ( $v$  has three components, and  $\sigma$  is a  $3 \times 3$  tensor) in Eq. (8) can be expressed as

$$\nabla \mathbf{w} \cdot \boldsymbol{\sigma} = \sum_{i,j=1}^3 \sigma_{ij} \partial_j w_i \approx \sum_{i,k=1}^3 \left( \sum_{j=1}^3 \sigma_{ij} \partial_j \xi_k \right) \frac{\partial w_i}{\partial \xi_k} = \sum_{i,k=1}^3 B_{ik} \frac{\partial w_i}{\partial \xi_k} \quad (31)$$

Through the interpolation and GLL integration of  $\partial w_i / \partial \xi_k$  in Eq. (31), the following is obtained

$$\begin{aligned} &\int_{\Omega^e} \nabla \mathbf{w} \cdot \boldsymbol{\sigma} d\mathbf{x} \\ &\approx \int_{-1}^1 \int_{-1}^1 \int_{-1}^1 \left[ \sum_{i,k=1}^3 B_{ik} \frac{\partial w_i}{\partial \xi_k} \right] \mathfrak{S} d\xi d\eta d\zeta \end{aligned} \quad (32)$$

$$= \sum_{i=1}^3 w_{i\alpha\beta\gamma} \left[ \begin{array}{l} \omega_\beta \omega_\gamma \sum_{l=0}^N \omega_l \mathfrak{T}_{l\beta\gamma} B_{i1l\beta\gamma} \ell'_\alpha \xi_l \\ + \omega_\alpha \omega_\beta \sum_{m=0}^N \omega_m \mathfrak{T}_{\alpha m\gamma} B_{i2\alpha m\gamma} \ell'_\beta \xi_m \\ + \omega_\alpha \omega_\beta \sum_{n=0}^N \omega_n \mathfrak{T}_{\alpha\beta n} B_{i3\alpha\beta n} \ell'_\beta \xi_n \end{array} \right] \quad (32)$$

## 2.6 Calculation of 3D seismic source

In most seismic studies, seismic source mechanism is described by the moment tensor  $\mathbf{M}_e$ . When describing a specific instance of earthquake, related information and focal mechanism solutions can be downloaded from the CMT website.

The seismic source term  $\mathbf{f}$  on the right side of Eq. (8) can be expressed as

$$\mathbf{f} = -\mathbf{M}_e \cdot \nabla \delta(\mathbf{x} - \mathbf{x}_s) S(t) \quad (33)$$

Where  $S(t)$  is the time function of seismic source, and  $\delta(\mathbf{x} - \mathbf{x}_s)$  is Dirac Delta distribution of seismic source. With the integral nature of the distribution, Moment tensor  $\mathbf{M}_e$  can be expressed as

$$\int_{\Omega^e} \mathbf{w} f dx = \mathbf{M}_e : \nabla \mathbf{w}(\mathbf{x}_s) S(t) \quad (34)$$

Where  $\mathbf{M}_e : \nabla \mathbf{w}$  can be calculated by the formula below

$$\begin{aligned} \mathbf{M}_e : \nabla \mathbf{w} &= \sum_{i,j=1}^3 M_{ij} \partial_j w_i \\ &\approx \sum_{i,k=1}^3 \left( \sum_{j=1}^3 M_{ij} \partial_j \xi_k \right) \frac{\partial w_i}{\partial \xi_k} = \sum_{i,k=1}^3 G_{ik} \frac{\partial w_i}{\partial \xi_k} \end{aligned} \quad (35)$$

As shown in Fig. 1, the seismic source is the point source, and  $\mathbf{x}_s = \mathbf{x}(\xi_{\alpha_s}, \xi_{\beta_s}, \xi_{\gamma_s})$ . Then the term on the right side of Eq. (8) can be calculated by the following formula

$$\mathbf{M}_e : \nabla \mathbf{w}(\mathbf{x}_s) = \sum_{i=1}^3 w_{i\alpha\beta\gamma} \left\{ \sum_{l,m,n=0}^N \left[ \begin{array}{l} \ell_\alpha(\xi_{\alpha_s}) \ell_\beta(\xi_{\beta_s}) \ell_\gamma(\xi_{\gamma_s}) \\ G_{(i)l\alpha\beta\gamma} \ell'_\alpha(\xi_{\alpha_s}) \ell'_\beta(\xi_{\beta_s}) \ell'_\gamma(\xi_{\gamma_s}) \\ + G_{(i2)l\alpha\beta\gamma} \ell_\alpha(\xi_{\alpha_s}) \ell'_\beta(\xi_{\beta_s}) \ell'_\gamma(\xi_{\gamma_s}) \\ + G_{(i3)l\alpha\beta\gamma} \ell_\alpha(\xi_{\alpha_s}) \ell_\beta(\xi_{\beta_s}) \ell'_\gamma(\xi_{\gamma_s}) \end{array} \right] \right\} \quad (36)$$

If  $\mathbf{x}_s$  coincides with GLL integration points, Eq. (36) can be simplified to

$$\mathbf{M}_e : \nabla \mathbf{w}(\mathbf{x}_s) \approx \sum_{i=1}^3 w_{(i)\alpha\beta\gamma} \begin{bmatrix} G_{(i1)\alpha_s\beta_s\gamma_s} \ell'_\alpha(\xi_{\alpha_s}) \delta_{\beta\beta_s} \delta_{\gamma\gamma_s} \\ + G_{(i2)\alpha_s\beta_s\gamma_s} \ell'_\beta(\xi_{\beta_s}) \delta_{\alpha\alpha_s} \delta_{\gamma\gamma_s} \\ + G_{(i3)\alpha_s\beta_s\gamma_s} \ell'_\gamma(\xi_{\gamma_s}) \delta_{\alpha\alpha_s} \delta_{\beta\beta_s} \end{bmatrix} \quad (37)$$

If the seismic source is located on the fault plane, the element boundary should be made coincident with the fault plane during mesh generation and  $\mathbf{M}_e : \nabla \mathbf{w} \mathbf{x}_s$  should be substituted by the following formula

$$\begin{aligned} \mathbf{M}_e : \nabla \mathbf{w} \mathbf{x}_s St &\rightarrow \int_{S_s} \mathbf{m}_e \mathbf{x}_s, \quad t: \nabla \mathbf{w} \mathbf{x}_s d^2 \mathbf{x}_s \\ &\approx \sum_{i=1}^3 w_{i\alpha\beta\gamma} \begin{bmatrix} \omega_\beta \sum_{\alpha_s=0}^N \omega_{\alpha_s} \mathfrak{T}^{\alpha_s\beta} g_{i1\alpha_s\beta\gamma} \ell'_\alpha \xi_{\alpha_s} \\ + \omega_\alpha \sum_{\beta_s=0}^N \omega_{\beta_s} \mathfrak{T}^{\alpha\beta_s} g_{i2\alpha\beta_s\gamma} \ell'_\beta \xi_{\beta_s} \\ + \omega_\alpha \omega_\beta \mathfrak{T}^{\alpha\beta} g_{i3\alpha\beta\gamma_s} \ell'_\gamma \xi_{\gamma_s} \end{bmatrix} \end{aligned} \quad (38)$$

In the equation above,  $g_{ik}$  can be obtained as follows

$$g_{ik} = \sum_{j=1}^3 m_{ij} \partial_j \xi_k \quad (39)$$

Where  $m_{ij}$  is density tensor of the moment;  $x_a, x_b$  represent grids on the fault plane, and  $x_g$  represents the grid perpendicular to the fault plane.

### 2.7 Global aggregate calculation

With the FEM for cell aggregation and the above derivation, calculation of the domain model shown in Fig. 1 can be expressed as

$$\mathbf{M}\ddot{\mathbf{U}} + \mathbf{C}\dot{\mathbf{U}} + \mathbf{K}\mathbf{U} = \mathbf{F} \quad (40)$$

Where  $\mathbf{M}$  is global mass matrix (see Eq. (26) for its derivation);  $\mathbf{U}$  is global displacement matrix;  $\mathbf{C}$  is global matrix of absorbing boundary (obtained by the integration of the second term in Eq. (7));  $\mathbf{K}$  is global stiffness matrix (obtained by the integration of the third term in Eq. (7)); and  $\mathbf{F}$  is seismic source.

## 3. Case study

### 3.1 The establishment of the model

The calculation region is 30.1°N-31.9°N and 102.35°E-103.15°E. With a length of 175.46 km in  $x$  direction and 196.46 km in  $y$  direction, it covers an area of 34471.41 km<sup>2</sup>, which is as shown

in Fig. 4. In Fig. 4(a), the area in blue box is the calculation region of this paper; the area in red box (Fig. 4(b)) near the seismic source is focus of this paper (As the earthquake occurred in this area before and the earthquake information was recorded clearly by the nearby monitoring stations, this area is selected as the calculation region. Besides, there are ridges, peaks, valleys, etc. in this area, which is helpful to research the influence of the different terrain on seismic wave.). The black triangles represent virtual stations, which are used to receive seismic signals from the program. They are located in the ridges, peaks, valleys, etc. The red five-pointed star represents the macroscopic epicenter and it coincides with ST3. Along the  $x$  and  $y$  directions, there are 96 spectral elements.  $z$  direction, based on LOH-3 reference model of the Pacific Earthquake Engineering Research Center, is divided into 15 spectral elements (Fig. 5). In the model, each spectral element contains 53 GLL points. Therefore, the model contains a total of 138,240 spectral elements, 9,088,756 mesh points, and a total degree of freedom of 27,266,268.

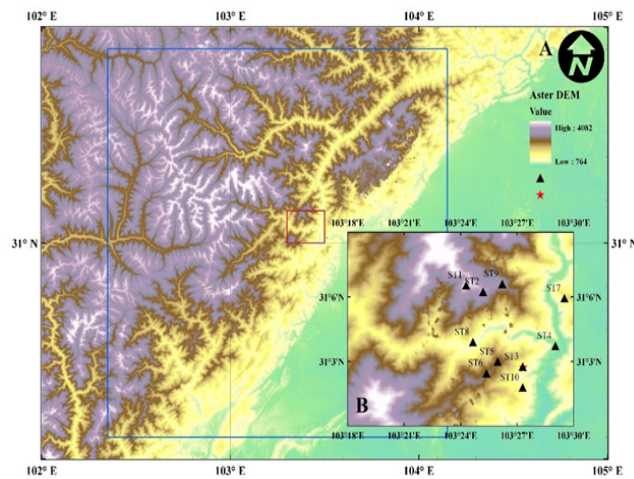


Fig. 4 Calculation region

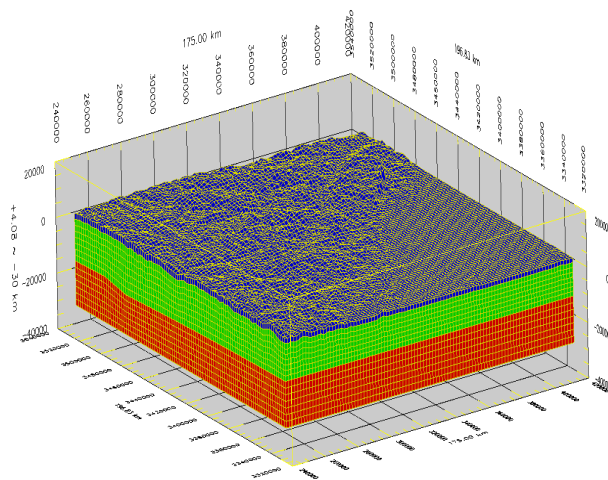


Fig. 5 Model calculation mesh

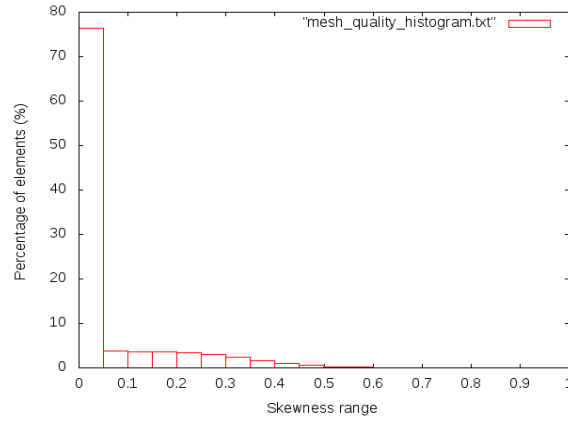


Fig. 6 Mesh quality histogram of model

Table 1 Model calculation parameters

Model number	$\rho/\text{kg}\cdot\text{m}^{-3}$	$v_p/\text{m}\cdot\text{s}^{-1}$	$v_s/\text{m}\cdot\text{s}^{-1}$	Number of spectrum element	$Q_\mu$
I	2600	4000	2000	1	40
II	2700	6000	3464	7	69.3
III	2950	6800	3800	7	76

Along the depth direction, the model is divided into three isotropic elastic bedrock materials. Velocity model is mainly based on P-wave velocity  $v_p$ ; S-wave velocity  $v_s$  and the quality factor  $Q_\mu$  are determined by the empirical formula (Brocher 2007).

$$\left. \begin{aligned} v_s &= (1.732 \sim 2)v_p \\ Q_\mu &= 0.02v_s \end{aligned} \right\} \quad (41)$$

As shown in Fig. 5, the blue grid is model I, the green grid is model II, and the red grid is model III. All the models represent the bedrock.

The mesh quality histogram of model is shown in Fig. 6. According to Fig. 6, it is easy to know that skewness values of most mesh are lower than 0.1.

Model calculation parameters are shown in Table 1.

In this paper, the SPEC3D SEM Program is the core code for calculation. The topographic effect and attenuation characteristics of the medium are taken into consideration. The calculation involves 6000 time steps and each step is 0.004 seconds. Therefore, it can simulate the propagation of seismic wave and its wave field in 24 seconds. In this calculation, eight computers with a total of 64 CPUs were used to perform parallel computing. It occupied about 16 Gb cluster memory and took about 6.8 h to complete. Generic Mapping tools (GMT) were used for data visualization and post-processing.

### 3.2 Seismic moment tensor solution and source time function

According to Eq. (33), the seismic source term can be solved by seismic moment tensor. The

```

PDE 2008 5 12 6 28 01.6 31.00 103.32 19.0 6.9 8.1 EASTERN SICHUAN, CHINA
event name: C200805120628A
time shift: 0.0000
half duration: 21.800
latitude: 31.4400
longitude: 104.1000
depth: 12.800
Mrr: 0.569000e+28
Mtt: 0.010000e+28
Mpp: -0.579000e+28
Mrt: -0.199000e+28
Mrp: 0.561000e+28
Mtp: -0.348000e+28

```



Fig. 7 Seismic moment parameters and focal mechanism solution of Wenchuan earthquake

point source moment tensor parameters and the focal mechanism solution of Wenchuan earthquake are shown in Fig. 7.

According to the moment tensor parameters in Fig. 7, seismic moment tensor  $\mathbf{M}_e$  (dyne·cm) is

$$\begin{aligned}
 \mathbf{M}_e &= \begin{bmatrix} M_{rr} & M_{r\theta} & M_{r\phi} \\ M_{r\theta} & M_{\theta\theta} & M_{\theta\phi} \\ M_{r\phi} & M_{\theta\phi} & M_{\phi\phi} \end{bmatrix} \\
 &= \begin{bmatrix} 0.569 \times 10^{28} & -0.199 \times 10^{28} & 0.561 \times 10^{28} \\ -0.199 \times 10^{28} & 0.01 \times 10^{28} & -0.348 \times 10^{28} \\ 0.561 \times 10^{28} & -0.348 \times 10^{28} & -0.579 \times 10^{28} \end{bmatrix}
 \end{aligned} \quad (42)$$

And the seismic scalar moment is

$$M_0 = \frac{1}{\sqrt{2}} (\mathbf{M}_e : \mathbf{M}_e)^{1/2} = 0.897 \times 10^{21} \text{ N}\cdot\text{m} \quad (43)$$

Eq. (43) shows that the released scalar moment is  $0.897 \times 10^{21} \text{ N}\cdot\text{m}$ .

In this paper, Gaussian function is adopted as the source time function of the point source.

$$f(t) = \frac{\alpha}{\sqrt{\pi\tau}} e^{-\left(\frac{at}{\tau}\right)^2} \quad (44)$$

Where  $\alpha$  is the delay rate of the seismic source, with a value of 1.628;  $\tau$  is the semi-duration of the seismic source (i.e., the value of the half duration in Fig. 7).

## 4. Analysis of three-dimensional topographic effects of ground motion

### 4.1 Post-processing of simulation results

Generic Mapping Tools (GMT) and Seismic Analysis Code (SAC2000) were used for data visualization and post-processing of simulation results. The former combined with bash script was mainly used for data processing and visualization, and the support of netCDF library was also needed; the latter was mainly used for processing of synthetic seismic wave signals and graphics

rendering.

The following steps shall be followed when using GMT to take wave field snapshots and post-process the peak ground acceleration distribution: Extract data (awk) → Convert raw data to netCDF format (xyz2grd) → Prepare the color palette (makecpt) based on numerical range → Resample (grdsample) → Draw the wave field and the peak ground acceleration distribution graphs or contour (grdimage or grdcontour), where texts in the parentheses are the Linux operating commands or GMT subroutines used in post-processing.

#### 4.2 Distribution of peak ground acceleration

Figs. 8-10 show the distribution of the peak ground acceleration (PGA), peak ground velocity (PGV) and peak ground displacement (PGD), respectively, in the epicenter area (Fig. 4(b)).

Fig. 8 shows that the maximum value of PGA in Fig. 4(b) is 1060  $\text{cm/s}^2$ , about 1.08 g. It is close to the value measured at Wolong Station, which to some extent verifies the accuracy of the

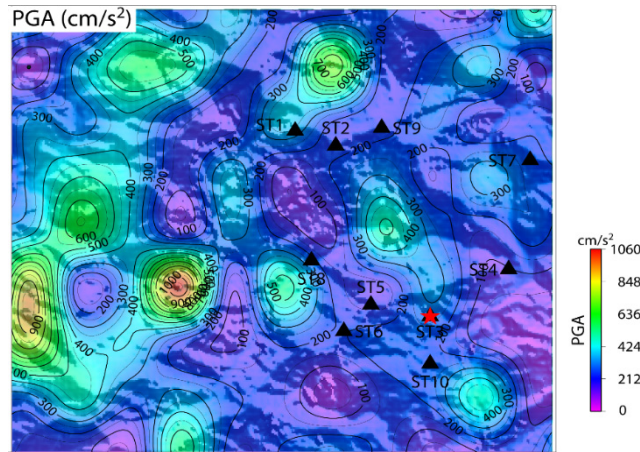


Fig. 8 Distribution of PGA

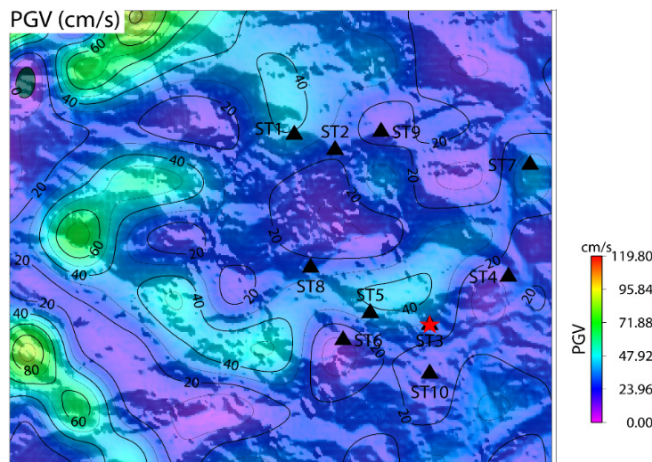


Fig. 9 Distribution of PGV

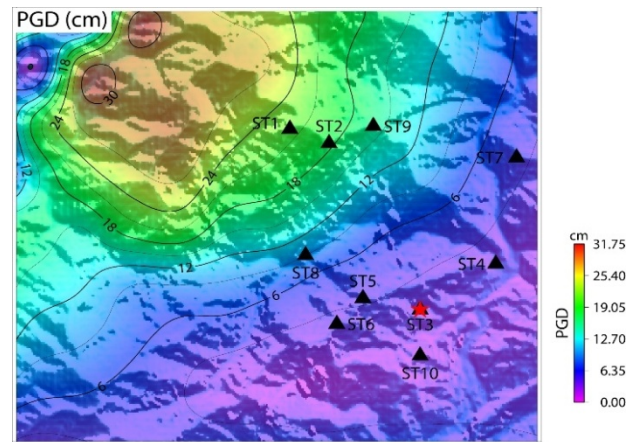


Fig. 10 Distribution of PGD

formula derivation and numerical simulation in this paper. The high PGA areas are distributed along the peak, the slope side away from the epicenter in the epicenter area, and a few ridges. The overall distribution direction of high PGA areas is parallel to the direction of the seismogenic fault. Meanwhile, the distribution of the high PGA areas is relatively discrete and most of them are located in the hanging wall of the seismogenic fault; there is also one high-profile PGA area at southeast ST10 in the footwall of the seismogenic fault, with a value of more than  $400 \text{ cm/s}^2$ .

Similar to the distribution of PGA, the high PGV areas are also discrete, as shown in Fig. 9. The overall distribution direction of high PGV region is also parallel to the direction of the seismogenic fault. In the southwest and northwest regions at higher elevations, high PGV values are observed, with the maximum being  $119.8 \text{ cm/s}$  throughout the region. As a whole, PGV values in the hanging wall of the seismogenic fault are greater than those in the footwall. It shows that there are significant differences between the ground motion in hanging wall and the footwall of the seismogenic fault.

In Fig. 10, the relationship between the distribution of PGD and the strike of the seismogenic fault is more clearly seen. All of the high PGD areas are located in the hanging wall of the seismogenic fault, with the maximum value,  $31.75 \text{ cm}$ , found on the summit of the northwest area. PGD values in the footwall of seismogenic fault are small, about  $5 \text{ cm}$ .

#### 4.3 Relative topographic amplification effect on ground motion

As can be seen from the distribution of PGA, PGV and PGD, the topographic amplification effect on ground motion is obvious. In order to further study such effect, the same seismic moment parameters are used in this paper for calculating the PGA distribution of the model without topographic term in the same region, as shown in Fig. 11.

The relative topographic amplification effect on PGA can be obtained by the following formula (Lee *et al.* 2009a, b)

$$AF_{PGA} = \frac{PGA_T - PGA_F}{PGA_F} \times 100\% \quad (45)$$

Where  $AF_{PGA}$  is the relative topographic magnification of PGA;  $PGA_T$  is the distribution of

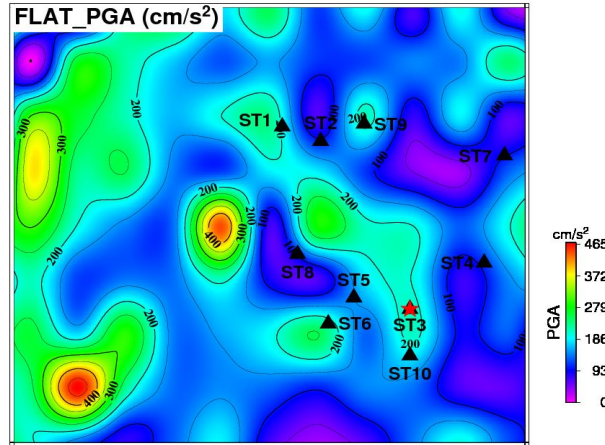


Fig. 11 PGA distribution of the model without topographic term

PGA of the real topographic model;  $PGA_F$  is the distribution of PGA of the model without local topography. Then according to Eq. (45), the relative magnification of PGA in the region shown in Fig. 4(b) is given in Fig. 12.

As shown in Fig. 12, the ground motion is amplified under the influence of the terrain in most of the area, generally by 10% to 20%. Distribution of the high relative amplification area is similar to that in Fig. 8, with most of the high relative amplification area near the ridge and the summit, while the negative relative amplification area is small. Distribution described above shows that the topographic amplification effect on PGA is extremely complex; it does not exactly lead to amplification of PGA at the ridge and the summit or attenuation of PGA in the valley. In Fig. 12, what should be noticed are the narrow negative relative amplification area between ST5 and ST3 and the negative relative amplification area along the ridge in the southwest. Compared with Fig. 8, although the region where the narrow area belongs to stretches over the ridge to the valley, it is a relatively low PGA distribution zone (only  $150\text{ cm/s}^2$ - $200\text{ cm/s}^2$ ).

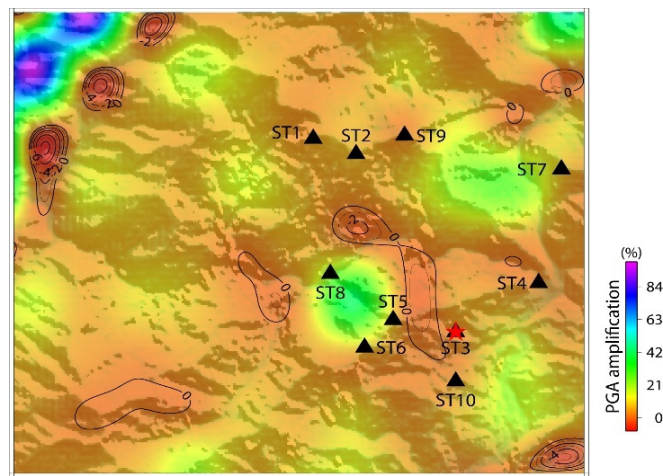


Fig. 12 PGA amplification under real terrain

## 5. Conclusions

The Spectral Element Method is a high-order Finite Element Method (FEM) characterized by high calculation accuracy and convergence speed. It can also be used to simulate the effect of complex terrain on seismic wave propagation.

- The Spectral Element Method (SEM) algorithm for simulation of 3D seismic wave propagation is derived based on the three-dimensional fluctuating elastic dynamic equation.
- The simulation results show that the high PGA areas are distributed along the peak and the slope side away from the epicenter. Their overall distribution direction is parallel to the direction of the seismogenic fault.
- The distribution of the high PGA areas is relatively discrete and most of them are located in the hanging wall of the seismogenic fault. The distribution of high PGD areas is also discrete, with an overall distribution direction parallel to the direction of the seismogenic fault. From the distribution of PGA, PGV and PGD areas, it is obvious that the terrain has certain amplification effect on the ground motion. Meanwhile, the topographic amplification effect on PGA is relatively complex. It does not exactly lead to amplification of PGA at the ridge and the summit or attenuation of PGA in the valley.

## Acknowledgments

Financial support for this paper was provided by the National Natural Science Foundation of China (41372356). The authors thank the anonymous referees for their careful reading of this paper and valuable suggestions.

## References

- Barani, S., Massa, M., Lovati, S. and Spallarossa, D. (2014), "Effects of surface topography on ground shaking prediction: implications for seismic hazard analysis and recommendations for seismic design", *Geophys. J. Int.*, **197**(3), 1551-1565.
- Brocher, T.M. (2007), "Key elements of regional seismic velocity models for long period ground motion simulations", *J. Seismol.*, **12**(2), 217-221.
- Chaljub, E., Maufroy, E., Moczo, P., Kristek, J., Hollender, F., Bard, P.Y., Priolo, E., Klin, P., de Martin, F., Zhang, Z.G., Zhang, W. and Chen, X.F. (2015), "3-D numerical simulations of earthquake ground motion in sedimentary basins: Testing accuracy through stringent models", *Geophys. J. Int.*, **201**(1), 90-111.
- Galvez, P., Ampuero, J.P., Dalguer, L.A., Somala, S.N. and Nissen-Meyer, T. (2014), "Dynamic earthquake rupture modelled with an unstructured 3-D spectral element method applied to the 2011 M9 Tohoku earthquake", *Geophys. J. Int.*, **198**(2), 1222-1240.
- Gao, Y. and Zhang, N. (2013), "Scattering of cylindrical SH waves induced by a symmetrical V-shaped canyon: near-source topographic effects", *Geophys. J. Int.*, **193**(2), 874-885.
- Gao, F.Z. and Zhao, G.Q. (2016), "Weak Galerkin finite element method for time dependent reaction-diffusion equation", *J. Computat. Anal. Appl.*, **21**(6), 1086-1102.
- Gao, X.W., Yuan, Z.C. and Peng, H.F. (2016), "Isoparametric closure elements in boundary element method", *Comput. Struct.*, **168**, 1-15.
- Komatitsch, D. and Tromp, J. (1999), "Introduction to the spectral element method for three-dimensional seismic wave propagation", *Geophys. J. Int.*, **139**(3), 806-822.
- Komatitsch, D. and Tromp, J. (2002), "Spectral-element simulations of global seismic wave propagation-I",

- Validat. Geophys. J. Int.*, **149**(2), 390-412.
- Lee, S.J., Chan, Y.C., Komatitsch, D., Huang, B.S. and Tromp, J. (2009a), "Effects of realistic surface topography on seismic ground motion in the Yangminshan region of Taiwan based upon the spectral-element method and Lidar DTM", *Bull. Seismol. Soc. Am.*, **99**(2), 681-693.
- Lee, S.J., Komatitsch, D., Huang, B.S. and Tromp, J. (2009b), "Effects of Topography on Seismic-Wave Propagation: An Example from Northern Taiwan", *Bull. Seismol. Soc. Am.*, **99**(1), 314-325.
- Liu, Q.F., Yu, Y.Y. and Zhang, X.B. (2015), "Three-dimensional simulations of strong ground motion in the Shidian basin based upon the spectral-element method", *Earthq. Eng. Eng. Vib.*, **14**(3), 385-398.
- Liu, Z.X., Liu, L. and Liang, J.W. (2016), "An indirect boundary element method to model the 3-D scattering of elastic waves in a fluid-saturated poroelastic half-space", *Eng. Anal. Bound. Elem.*, **66**, 91-108.
- Meunier, P., Hovius, N. and Haines, J.A. (2008), "Topographic site effects and the location of earthquake induced landslides", *Earth Planet. Sci. Lett.*, **275**(3-4), 221-232.
- Rizzitano, S., Cascone, E. and Biondi, G. (2014), "Coupling of topographic and stratigraphic effects on seismic response of slopes through 2D linear and equivalent linear analyses", *Soil Dyn. Earthq. Eng.*, **67**, 66-84.
- Shao, Y.B. and Ma, W.Y. (2016), "Finite difference approximations for the two-side space-time fractional advection-diffusion equations", *J. Computat. Anal. Appl.*, **21**(2), 369-379.
- Sugan, M. and Vuan, A. (2014), "On the ability of Moho reflections to affect the ground motion in northeastern Italy: A case study of the 2012 Emilia seismic sequence", *Bull. Earthq. Eng.*, **12**(5), 2179-2194.
- Tarinejad, R. and Pirboudaghi, S. (2015), "Legendre spectral element method for seismic analysis of dam-reservoir interaction", *Int. J. Civil Eng.*, **13**(2A), 148-159.
- Todorovska, M.I., Trifunac, M.D., Ding, H.P. and Orbovic, N. (2015), "Coherency of dispersed synthetic earthquake ground motion at small separation distances: Dependence on site conditions", *Soil Dyn. Earthq. Eng.*, **79**, 253-264.
- Udias, A. (2008), *Principles of Seismology*, Cambridge University Press, New York, NY, USA.
- Yan, Z.Z., Zhang, H., Yang, C.C. and Shi, Y.L. (2009), "Spectral element analysis on the characteristics of seismic wave propagation triggered by Wenchuan Ms 8.0 earthquake", *Science in China Series D: Earth Sciences*, **52**(6), 764-773.
- Yoshimatsu, H. and Abe, S. (2006), "A review of landslide hazards in Japan and assessment of their susceptibility using an analytical hierarchic process (AHP) method", *Landslides*, **3**(2), 149-158.
- Zhang, N., Gao, Y.F., Yang, J. and Xu, C.J. (2015), "An analytical solution to the scattering of cylindrical SH waves by a partially filled semi-circular alluvial valley: Near-source site effects", *Earthq. Eng. Eng. Vib.*, **14**(2), 189-201.
- Zhao, M., Yin, H.Q., Du, X.L., Liu, J.B. and Liang, L.Y. (2015), "1D finite element artificial boundary method for layered half space site response from obliquely incident earthquake", *Earthq. Struct., Int. J.*, **9**(1), 173-194.